



Article

Influence of CFD Modelling Parameters on Air Injection Behaviour in Ship Air Lubrication Systems

Gyeongseo Min ¹, Haechan Yun ¹, Younguk Do ¹, Kangmin Kim ¹, Keounghyun Jung ¹, Saishuai Dai ², Mehmet Atlar ², Daejeong Kim ³, Seungnam Kim ⁴ , Sanghyun Kim ^{1,*} and Soonseok Song ^{1,*} 

¹ Department of Naval Architecture & Ocean Engineering, Inha University, Incheon 22212, Republic of Korea; gyeongseo6691@naver.com (G.M.)

² Department of Naval Architecture, Ocean and Marine Engineering, University of Strathclyde, Glasgow G1 1XQ, UK

³ Division of Navigation Convergence Studies, Korea Maritime & Ocean University, Busan 49200, Republic of Korea; kdj4907@kmou.ac.kr

⁴ Department of Naval Architecture and Ocean Engineering, Hongik University, Seoul 04066, Republic of Korea; naoestar@hongik.ac.kr

* Correspondence: kimsh@inha.ac.kr (S.K.); s.song@inha.ac.kr (S.S.)

Abstract

In response to the International Maritime Organization's strengthened regulations on carbon emissions, the introduction of novel eco-friendly technologies for ship operators has become necessary. In this context, various energy saving devices such as wind-assisted propulsion systems (e.g., wing/rotor sails), propeller-rudder efficiency enhancers (e.g., pre-swirl stators or ducted propellers), and the gate rudder system have been proposed. Among various energy-saving technologies, the air lubrication system has been widely investigated as an effective means of reducing hull frictional resistance through air injection beneath the hull. The performance of air lubrication systems can be evaluated through experimental testing or computational fluid dynamics (CFD) simulations. However, accurately simulating air lubrication systems in CFD remains challenging. Therefore, this study aims to quantitatively evaluate the influence of numerical parameters on the CFD implementation of air lubrication systems. To evaluate these influences, CFD simulations employing the unsteady Reynolds-averaged Navier–Stokes (URANS) method were conducted to investigate air layer formation and sweep angle on a flat plate. The numerical predictions were systematically compared with experimental results by varying key numerical parameters. These quantitative estimations of the effects of numerical variables are expected to serve as a useful benchmark for CFD simulations of air lubrication systems.

Keywords: air lubrication system (ALS); computational fluid dynamics (CFD); energy saving device (ESD); drag reduction



Academic Editor: Kostas Belibassakis

Received: 3 January 2026

Revised: 20 January 2026

Accepted: 21 January 2026

Published: 22 January 2026

Copyright: © 2026 by the authors.

Licensee MDPI, Basel, Switzerland.

This article is an open access article distributed under the terms and conditions of the [Creative Commons Attribution \(CC BY\) license](https://creativecommons.org/licenses/by/4.0/).

1. Introduction

Recently, climate change driven by carbon emissions has become a significant global issue. Given that ships account for a substantial share of global trade, the maritime sector also contributes notably to carbon emissions. In response, the International Maritime Organization (IMO) has introduced carbon reduction strategies, aiming for a 20–30% decrease in emissions by 2030 and a 70–80% reduction by 2040 relative to 2008 levels, with a goal of achieving net-zero emissions by 2050 [1]. These strengthened IMO regulations on carbon emissions inevitably require substantial technological changes in existing vessels.

In accordance with these regulatory demands, one technological response has been the adoption of new energy-saving devices. Various types of energy-saving devices have been proposed and investigated. One example is wind-assisted ship propulsion (WASP) technologies, which harness wind power for auxiliary propulsion through devices such as rotor sails, wing sails, and kite systems [2–4]. Another type of energy-saving device is designed to minimize various forms of energy loss. These devices include pre-swirl stators (PSSs) and pre-swirl ducts (PSDs) for improving propeller efficiency, as well as air lubrication systems (ALSs) for reducing hull resistance [5]. Among the diverse range of energy-saving devices available, the present study focuses specifically on ALS technology.

The air lubrication system (ALS) is a resistance-reduction technology that operates by injecting air onto the hull bottom, forming an air layer on the hull surface that reduces frictional resistance. Furthermore, this technology was first successfully applied to commercial vessels in 2010 [6,7]. In this context, various previous studies have examined the application of air lubrication system to ships [8–12]. The first approach to evaluating air lubrication system is through experimentation. Gas pocket morphology with air injection at a single inlet was estimated by varying the free-stream velocity, injection orifice diameter, and injection rate [13]. Furthermore, air layer formation on a flat plate was observed through experiments conducted in the cavitation tunnel of the Samsung Ship Model Basin (SSMB) [14]. Also, the power-saving effect was estimated via resistance and self-propulsion tests with ALS applied to a 66K DWT Supramax bulk carrier model. Additionally, an experimental study on ALS application to tanker models has also been conducted [15]. Another way to evaluate the efficiency of air lubrication systems is through computational fluid dynamics (CFD). As a fundamental study prior to ship-scale application, the variation in sweep angle of the air layer and frictional resistance on a flat plate was assessed using CFD and compared with experimental data [16]. Building upon these fundamental studies, CFD research for actual ship applications has been actively conducted [17–20]. For example, based on CFD simulations of frictional resistance, a new extrapolation method was proposed for ships equipped with air lubrication systems [21,22].

Accordingly, implementing air lubrication systems through CFD requires accurately capturing the boundary between the air layer and water formed at the hull bottom, which is an important aspect of such applications. There are two modelling approaches that capture this boundary between the two phases, including the Volume of Fluid (VOF) and the Eulerian Multi-Phase (EMP) methods. The difference between the two methods is whether interpenetration of the two phases is allowed [23]. First, the VOF model assumes that two fluids are immiscible and tracks the interface by solving the continuity equation, the momentum equation, and transport equations for the volume fraction of each phase. In contrast, the EMP model allows interpenetration of the two phases, representing each phase with own volume fraction and solving separate momentum and transport equations for each phase.

As a result of comparing the differences when applying these two models, a previous study observed that the VOF model tends to overestimate the drag reduction effect compared to the EMP model when evaluating the drag reduction rate [16]. Therefore, based on these findings, a subsequent numerical study was performed to estimate frictional resistance employing the EMP model with a double-body approach [24]. However, this approach using the double-body model has a limitation that it cannot account for free surface effects. Consequently, the VOF model remains essential for comprehensive ALS performance evaluation due to its capability to consider free surface effects and applicability to various simulation scenarios. However, despite its extensive application in ALS research, systematic quantitative analysis of how individual numerical parameters, such as time step, turbulence model, wall treatment, and interface capturing scheme, affect the accuracy

and reliability of VOF-based ALS simulations has been lacking in previous studies. In this regard, the present study aims to fill this research gap by developing a methodology using the VOF model to evaluate the performance of the air lubrication system that can be extended to various types of simulations. To accomplish this, a parametric study was conducted by varying key numerical variables across multiple aspects, encompassing the VOF methods presented in previous studies, to compare the sweep angle of the air layer on a flat plate against experimental results and assess the drag reduction rate. However, it should be noted that this study uses a simplified flat plate with a single injection hole, whereas actual ships employ multiple injection holes in slit configurations with complex hull geometries. Despite these simplifications, this approach enables systematic parametric investigation and provides fundamental numerical guidelines for ALS implementation in CFD.

This paper is structured as follows: Section 2 presents the methodology of this study including the mathematical formulations and boundary conditions of the computational domain for numerical simulations. Validation study through comparison with experimental data and verification study for uncertainty estimation are addressed in Section 3. Finally, the effect of numerical variables on the formation of the air layer and drag reduction rate is presented in Section 4.

2. Methodology

2.1. Mathematical Formulation

A CFD model for evaluating the influence of numerical variables on the implementation of an air lubrication system was developed using the commercial CFD software package, STAR-CCM+ (version 19.06.008). This software implements the unsteady Reynolds-averaged Navier–Stokes (URANS) approach, which resolves the averaged continuity and momentum equations for incompressible flow through following equations expressed in tensor notation within Cartesian coordinates [25].

$$\frac{\partial \rho}{\partial t} + \frac{\partial(\rho \bar{u}_i)}{\partial \bar{x}_i} = 0 \quad (1)$$

$$\frac{\partial(\rho \bar{u}_i)}{\partial t} + \frac{\partial}{\partial x_j} (\rho \bar{u}_i \bar{u}_j + \rho \overline{u'_i u'_j}) = -\frac{\partial \bar{p}}{\partial x_i} + \frac{\partial \bar{\tau}_{ij}}{\partial x_i} \quad (2)$$

In these equations, ρ , \bar{u}_i , $\overline{u'_i u'_j}$, \bar{p} , and $\bar{\tau}_{ij}$ respectively denote the density, averaged velocity, Reynolds stress, averaged pressure, and mean viscous stress tensor components. Furthermore, for Newtonian fluid, this viscous stress can be written as

$$\bar{\tau}_{ij} = \mu \left(\frac{\partial u_i}{\partial x_j} + \frac{\partial u_j}{\partial x_i} \right) \quad (3)$$

where μ denotes the dynamic viscosity of fluid.

The numerical simulations were conducted using the finite volume method by discretizing the computational domain. For the pressure-velocity coupling, a Semi-Implicit Method for Pressure-Linked Equations (SIMPLE) algorithm was employed. Furthermore, in this study, numerical variables were systematically varied to investigate their effects on air layer formation and drag reduction rate. To achieve this, the momentum equation was solved using a second-order upwind convection scheme. Temporal discretization was conducted through comparative analysis of first-order and second-order schemes to evaluate their differences. Additionally, the effect of turbulence model was also systematically investigated by varying specific turbulence models, including the shear stress transport (SST) $k - \omega$, realizable $k - \epsilon$, and Reynolds stress transport (RST) models. To capture

the boundary between air and water, the Volume of Fluid method with High-Resolution Interface Capturing (HRIC) was applied. In particular, the influence of numerical diffusion was comprehensively estimated by varying the parameters that reduce numerical diffusion in HRIC. In this study, the boundary between air and water was tracked using an iso-surface function to identify the interface between two phases, specifically by locating the iso-surface at volume fraction 0.5 where water and air are equally mixed.

2.2. Geometry and Boundary Conditions

In this study, the effects of different numerical variables on air layer formation were evaluated by comparing the experimental results conducted using a barge ship equipped with an air lubrication system [13]. The configuration of the barge ship with the air lubrication system used in the experiment is illustrated in Figure 1. Since previous CFD studies on air layer formation have demonstrated that the effect of hull geometry on air layer characteristics such as sweep angle is negligible [16], the numerical simulation was conducted using a simplified flat plate geometry to represent the bottom of the barge ship. Specifically, the boundary conditions of the computational domain were depicted in Figure 2. Furthermore, the main particulars of the air lubrication system are presented in Table 1. All velocity inlets shown in Figure 2 correspond to water flow entering in the positive x-axis direction with the free-stream velocity specified in Table 1 (2 m/s). The air injection is modelled through the mass flow inlet indicated in red in Figure 2, with the flow rate condition specified in Table 1. These conditions were identical to those used in the experiment, and the direction of air injection was maintained perpendicular to the plate, consistent with the experiment. Furthermore, regarding the initial conditions, the simulation begins with an established flow field where air is generated through the mass flow inlet. For the volume fraction field, water only is initialized at all velocity inlets flowing in the aforementioned direction, while air only is generated at the mass flow inlet.

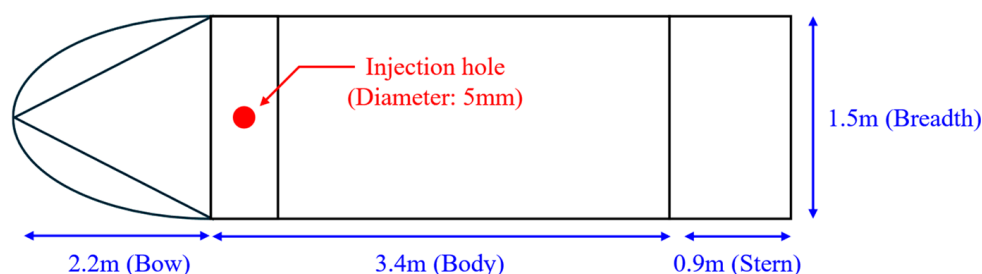


Figure 1. Geometry of a barge ship with an air lubrication system.

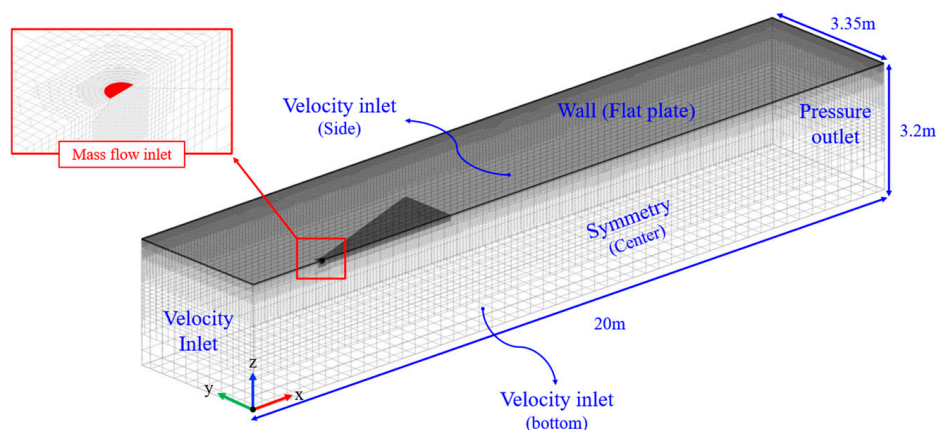


Figure 2. Configuration of numerical domain and boundary conditions.

Table 1. Parameters of air lubrication system.

Main Parameters	
Injection hole diameter	5 mm
Free-stream speed	2 m/s
Air injection rate	$2.0 \times 10^{-3} \text{ m}^3/\text{s}$

2.3. Sweep Angle Definition and Resistance Approach

The effects of key variables in air layer formation in CFD were analyzed by varying time step, temporal discretization order, sharpening factor, turbulence models, and the value of wall y^+ across different cases, measuring the sweep angle of the formed air layer and the drag reduction on the flat plate. First, the definition of sweep angle can be found in Figure 3. As shown in Figure 3, the sweep angle was measured as the distance from the injection hole to the point where the iso-surface of volume fraction of water reaches 0.5, located 1.5 m downstream of the injection hole. This method was presented in a previous study [13,16]. Physically, although the air layer boundary is instantaneously irregular, this measurement approach effectively captures the overall air distribution pattern.

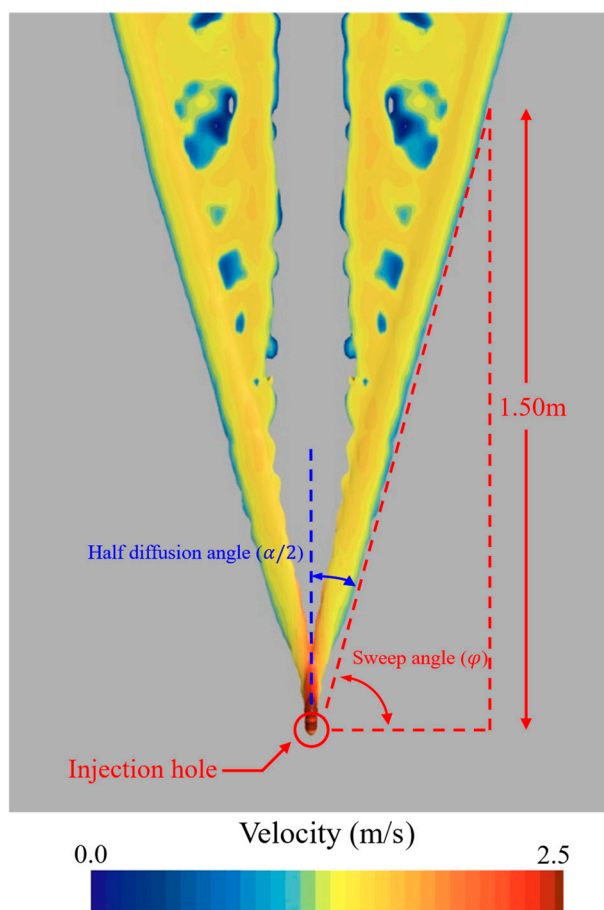


Figure 3. Definition of sweep angle for air layer formation measurement.

Furthermore, drag reduction rates of each case were also presented in this paper. These quantified estimations represented the drag measured specifically on the blue-highlighted section shown in Figure 4. This measurement section was the corresponding area excluding the bow section of the barge ship model in Figure 2. The drag reduction rate was quantified from the total resistance including both frictional and pressure components measured on this highlighted section. Although drag reduction rates were not presented in the

experimental study, this study additionally evaluated them, considering that a previous study using the VOF method reported a tendency to overestimate drag reduction [13,24]. Since experimental drag data were not available for validation, the reliability of the drag predictions was ensured through the grid convergence test conducted in Section 3.2. The sweep angle and drag measurements were monitored until their variation rates converged to within 1%, after which observations continued for more than 10 s. The final 10 s interval of this converged period was used for data collection and analysis. To ensure that a statistical steady state was reached, simulations were run for more than 200 s.

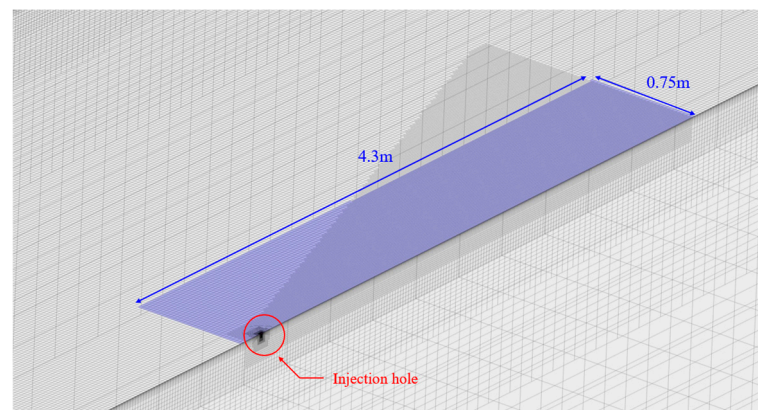


Figure 4. Resistance measurement section of flat plate for drag reduction rate estimation.

2.4. Mesh Generation

The grid system for the computational domain was generated using the automatic meshing tool in STAR-CCM+ (version 19.06.008). Specifically, trimmed cell meshes were employed to construct the grid system. Furthermore, prism layers were applied near the flat plate surface to accurately resolve the boundary layer. In Sections 4.1 and 4.2, the height of the first prism layer was configured to maintain a wall y^+ value greater than 30. However, in Section 4.3, an additional case with the first cell height adjusted to achieve a wall y^+ value below 1 was also examined to compare the effect of wall y^+ on the simulation results. As shown in Figures 2 and 4, prism layers were applied around the flat plate, and local mesh refinement was implemented near the injection hole within the diffusion angle region to accurately capture the interface between the air and water phases during air injection. Moreover, in this study, the mesh around the plate was configured to ensure that the Courant–Friedrichs–Lewy (CFL) number remained below 1 even at the largest time step of 0.02 s used in the parametric study.

3. Validation and Verification Studies

3.1. Validation Through Comparison with Experimental Data

In this section, a validation study was conducted by comparing experimental data with CFD simulations [13]. The experimental study employed various conditions including different air flow rates, injection hole sizes, and free-stream velocities. Among these conditions, the present study selected and validated the case with a free-stream velocity of 2 m/s, air injection rate of $2.0 \times 10^{-3} \text{ m}^3/\text{s}$, and injection hole diameter of 5 mm for comparison. As depicted in Figure 5, a comprehensive comparative analysis revealed that the air layer morphology obtained from experimental data closely aligned with the air layer morphology predicted by CFD. Furthermore, a quantitative assessment of the air layer formation was performed through comparative analysis of the air layer's sweep angle.

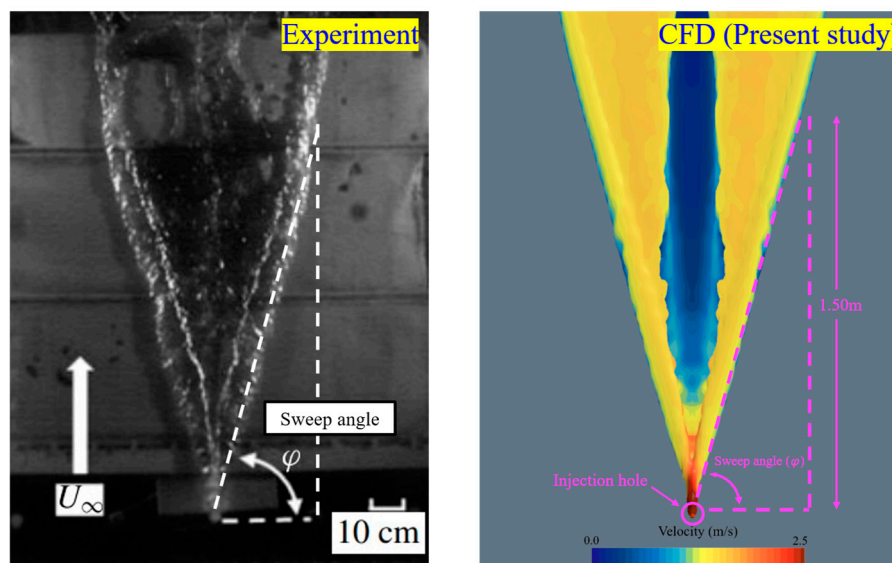


Figure 5. Comparative analysis of air layer between EFD and CFD.

As presented in Table 2, the difference in sweep angle between the EFD and CFD showed a deviation of less than 1%. To provide additional cross-validation, CFD results from a previous study [16] were also included in Table 2 for comparison, demonstrating good agreement with the present results. It should be noted that these simulation results represent the optimal outcomes identified through a parametric study of numerical variables, which demonstrated the closest agreement with experimental data. The simulations used a time step of 0.001 s, second-order temporal discretization, a sharpening factor of 0, y^+ values below 1, and the SST $k - \omega$ turbulence model. These optimal parameter settings were determined through the systematic studies presented in Section 4. Furthermore, total resistance was also a significant evaluation parameter in the ALS. However, as previously mentioned, the resistance values were not reported in the experiment, and therefore reliability was ensured through the uncertainty analysis conducted in Section 3.2.

Table 2. Quantitative estimation of the sweep angle between the EFD and CFD.

	EFD	CFD (Present Study)	CFD (Previous Study)
Sweep angle	74.2°	74.79°	78.5°
Difference		0.80%	5.80%

3.2. Uncertainty Estimation Through Grid Convergence Test

In addition to the validation study, a verification study was conducted through grid convergence tests. Specifically, the Grid Convergence Index (GCI) method was employed to assess numerical uncertainty, which was estimated for two key variables of the air layer, namely the sweep angle and the total resistance on the flat plate [26]. This study performed simulations under two meshing conditions with wall y^+ greater than 30 and wall y^+ less than 1, consistent with the numerical settings used in the validation study presented in Section 3.1. Grid convergence tests were conducted for both conditions to ensure numerical reliability. Moreover, three grid levels (coarse, medium, and fine) were employed, which is the standard minimum requirement for grid convergence studies. While the sweep angle could be directly validated against experimental data as demonstrated in the previous section, drag data were not provided in the experiments. Therefore, the reliability of drag predictions was established through the grid convergence tests conducted in this section. Both key variables exhibited a tendency to converge with increasing number of

cells regardless of the wall y^+ condition. Furthermore, quantitative estimation of numerical uncertainty revealed values below 1% for both key variables under both meshing strategies, as presented in Table 3 and Appendix A.

Table 3. Uncertainty estimation through grid convergence tests.

Wall $y^+ > 30$	No. Cells	Sweep Angle (deg)	C_T
	1,183,389	75.61	1.635×10^{-3}
	2,096,642	73.83	1.511×10^{-3}
	3,039,828	74.24	1.525×10^{-3}
	GCI_{fine}	0.37%	0.39%
Wall $y^+ < 1$	No. Cells	Sweep Angle (deg)	C_T
	1,155,243	76.16	1.364×10^{-3}
	2,572,342	74.87	1.256×10^{-3}
	4,412,050	74.79	1.253×10^{-3}
	GCI_{fine}	0.02%	0.03%

Given these convergence characteristics, subsequent analyses were conducted using the fine mesh for both cases. In principle, an uncertainty test with respect to time should be conducted through a temporal convergence test. Since the time step was also part of the parametric study in this work, a temporal convergence test was performed separately in Section 4.1 to determine an appropriate time step. Therefore, only a spatial convergence test is presented in this section.

4. Result

4.1. Effects of Time Step and Time Discretization Order

In this section, the influences of the following numerical parameters on the CFD simulation of an ALS were assessed:

- Time step size.
- Temporal discretization order.

As presented in Table 4, five time steps (0.02 s, 0.01 s, 0.002 s, 0.001 s, and 0.0005 s) and two time discretization schemes (first and second order) were examined, resulting in 10 cases in total. The SST $k - \omega$ turbulence model and the high wall y^+ approach (i.e., $y^+ > 30$) were employed for all cases based on the findings from the previous study [16]. For each case, the air layer formation and drag reduction effects produced by the air lubrication system were evaluated.

First, the influences of parameter variations on air layer formation were assessed. Figure 6 illustrates the air layer generated beneath the plate, visualized through an iso-surface corresponding to a water volume fraction of 0.5. When employing the first-order temporal discretization scheme, enhanced air layer formation was observed with decreasing time step size. Similarly, for the second-order temporal discretization scheme, stable air layer formation was achieved at smaller time steps.

The effects of temporal discretization scheme were most evident in the time step requirement for stable air layer formation. The first-order scheme required the smallest time step of 0.0005 s to achieve stability, while the second-order scheme maintained stability at the relatively larger time steps of 0.001 s or smaller. Additionally, as shown in Figure 6, the second-order temporal discretization scheme produced a more uniform air layer compared to the first-order scheme at equivalent time steps. For quantitative evaluation of the air layer formation characteristics, the differences in sweep angle from the experimental results

were assessed, as presented in Table 4 and Figure 7 [13]. It should be noted that cases with insufficient air layer formation could not be evaluated.

Table 4. Effects of temporal discretization parameters on sweep angle and resistance of air layer.

	Case 1.1	Case 1.2	Case 1.3	Case 1.4	Case 1.5
Temporal order	First	First	First	First	First
Time step	0.02 s	0.01 s	0.002 s	0.001 s	0.0005 s
Sweep angle (deg)	80.96	80.53	78.90	76.03	74.94
Error (%)	9.11	8.53	6.33	2.46	1.00
C_T	2.279×10^{-3}	2.278×10^{-3}	2.109×10^{-3}	1.796×10^{-3}	1.665×10^{-3}
Drag reduction rate (%)	7.74	7.78	14.63	27.22	32.58
	Case 1.6	Case 1.7	Case 1.8	Case 1.9	Case 1.10
Temporal order	Second	Second	Second	Second	Second
Time step	0.02 s	0.01 s	0.002 s	0.001 s	0.0005 s
Sweep angle (deg)	N/A	N/A	75.34	74.24	73.97
Error (%)	N/A	N/A	1.54	0.051	0.31
C_T	2.324×10^{-3}	2.227×10^{-3}	1.753×10^{-3}	1.526×10^{-3}	1.530×10^{-3}
Drag reduction rate (%)	5.92	9.85	29.04	38.21	38.05

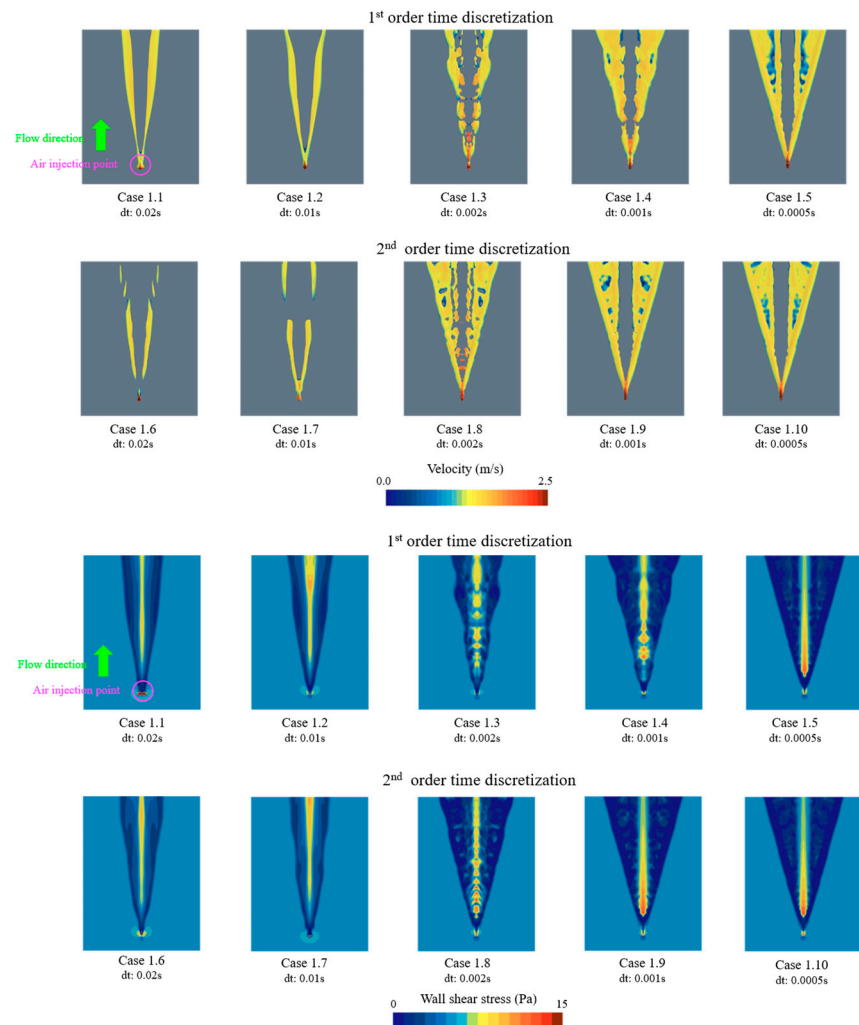


Figure 6. Effects of temporal discretization parameters on air layer formation and shear stress on the plate.

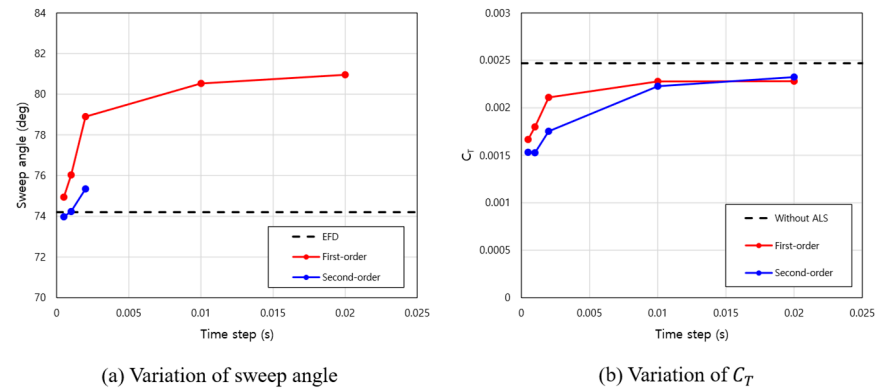


Figure 7. Comparison of sweep angle and C_T under different numerical modelling conditions.

In most cases with larger time steps, the sweep angle was overestimated relative to the experimental value of 74.2° , indicating a smaller diffusion angle. Furthermore, similar to the air layer formation trends, improved agreement with experimental results was observed with increased computational cost through smaller time steps. As a result, Case 1.9 achieved significantly improved agreement with the experiment, with an error of only 0.051%.

Furthermore, the drag reduction effect for each case was quantitatively evaluated, as presented in Table 4 and Figure 7. Although the experiment did not provide the resistance of the flat plate or the corresponding drag reduction rates, these values were additionally calculated in the present study to facilitate a more comprehensive assessment of the effectiveness of the air lubrication system. As a baseline, considering a free stream velocity of 2 m/s and a measurement area of 6.45 m^2 on the flat plate, the total resistance coefficient without air injection was determined to be 2.47×10^{-3} . The quantitative evaluation of the drag reduction effect showed a good correlation with air layer formation. Cases with more stable air layer formation exhibited greater drag reduction. Furthermore, the variation in shear stress, as shown in Figure 6, revealed additional effects that contributed to the changes in drag reduction rate, which could not be captured by comparing the sweep angles of the air layer alone.

Based on these results, it was confirmed that the most stable air layer was formed when the time step was set to 0.0005 s for the first-order scheme (Case 1.5) and 0.001 s for the second-order scheme (Case 1.9 and Case 1.10). Furthermore, considering the similar air layer quality at time steps of 0.001 s and 0.0005 s for the second-order scheme, and comparable results to the first-order scheme at 0.0005 s, a time step of 0.001 s with the second-order scheme was selected to reduce computational cost for the comparison of other numerical parameters. To validate this selection, a time step convergence test was conducted for the case using the second-order temporal discretization scheme, which produced the most similar air layer formation to the experiment, as shown in Table 5 [26].

Table 5. The results of time step convergence test.

Temporal Convergence Test	dt	Sweep Angle (deg)	C_T
Coarse	0.002 s	75.34	1.753×10^{-3}
Medium	0.001 s	74.24	1.526×10^{-3}
Fine	0.0005 s	73.97	1.530×10^{-3}
GCI_{mid}		0.59%	0.33%

Moreover, the comparison between the two temporal orders showed differences in both the smoothness of air layer formation and the drag reduction rate. This raises the question of why such differences exist between the two temporal discretization schemes. The present study addressed this question by noting that the two temporal discretization orders differ in the accuracy of grid flux computation, which in turn affects the degree of numerical diffusion. Specifically, all simulations in Part 1 of this section were performed without any additional settings to reduce numerical diffusion. However, according to the user guide of STAR-CCM+, the commercial software used in the present study, employing the second-order temporal discretization scheme can effectively reduce numerical diffusion without requiring additional settings [27]. Based on these results, it was confirmed that numerical diffusion influences air layer formation. Therefore, this effect was further evaluated in Section 4.2.

4.2. Influence of Time Discretization Order and Numerical Diffusion

Following the analysis conducted in Section 4.1, the present section investigates how numerical diffusion affects the development of the air layer by adjusting the sharpening factor parameters. Based on the findings from Section 4.1, the time step was fixed at 0.001 s to ensure accurate air layer formation.

In this subsection, numerical diffusion was controlled through the sharpening factor implemented in the HRIC scheme. Specifically, the sharpening factor, bounded between 0.0 and 1.0, functions to suppress numerical diffusion within the simulation. At the maximum value of 1.0, numerical diffusion is effectively eliminated, resulting in a distinctly sharp interface between the two phases [27].

$$\frac{\partial}{\partial t} \int_V \alpha_i dV + \oint_A \alpha_i v \cdot da = \int_V \left(S_{\alpha_i} - \frac{\alpha_i}{\rho_i} \frac{D\rho_i}{Dt} \right) dV - \int_V \frac{1}{\rho_i} \nabla \cdot (\alpha_i \rho_i v_{d,i}) dV \tag{4}$$

When the sharpening factor is zero, the phase mass conservation equation is expressed as Equation (4). In this equation, α_i , v , S_{α_i} , ρ_i , $v_{d,i}$, and $\frac{D\rho_i}{Dt}$ denote the volume fraction of phase i , mass-averaged velocity, user-defined source term of phase i , density of phase i , diffusion velocity, and Lagrangian derivative of the phase density, respectively. In the present study, water and air are used as the phase, and thus these two phases correspond to the user-defined source term of phase. However, when the sharpening factor assumes a non-zero value, Equation (4) is modified to Equation (5), where C_α represents the sharpening factor. Additionally, as the sharpening factor increases, it plays a role in suppressing numerical diffusion.

$$\frac{\partial}{\partial t} \int_V \alpha_i dV + \oint_A \alpha_i v \cdot da = \int_V \left(S_{\alpha_i} - \frac{\alpha_i}{\rho_i} \frac{D\rho_i}{Dt} \right) dV - \int_V \frac{1}{\rho_i} \nabla \cdot (\alpha_i \rho_i v_{d,i}) dV + \nabla \cdot (C_\alpha |v| \frac{\nabla \alpha_i}{|\alpha_i|} \alpha_i (1 - \alpha_i)) \tag{5}$$

Furthermore, for assessing the effects of numerical diffusion, air layer formation and drag reduction rates were evaluated for six cases with different temporal discretization orders and sharpening factors, as summarized in Table 6. In these cases, the time step was set to 0.001 s, based on the stable air layer formation conditions determined in Section 4.1. Additionally, Case 2.1 and Case 2.4, where the sharpening factor is set to zero, are identical to Case 1.4 and Case 1.9 from Section 4.1, respectively. As in Section 4.1, all cases were simulated using the SST $k - \omega$ turbulence model with wall y^+ values maintained above 30.

Table 6. Effects of temporal discretization order and sharpening factor on sweep angle and resistance of a plate.

	Case 2.1	Case 2.2	Case 2.3	Case 2.4	Case 2.5	Case 2.6
Temporal order	First	First	First	Second	Second	Second
Sharpening factor (C_α)	0.0	0.3	0.5	0.0	0.3	0.5
Sweep angle (deg)	76.03	73.74	70.65	74.24	71.24	70.98
Error (%)	2.46	0.63	4.79	0.051	3.99	4.33
C_T	1.796×10^{-3}	1.298×10^{-3}	1.693×10^{-3}	1.526×10^{-3}	1.757×10^{-3}	1.831×10^{-3}
Drag reduction rate (%)	27.22	47.46	31.45	38.21	28.86	25.85

As depicted in Figure 8, the shape of the air layer varied with different temporal discretization orders and sharpening factors. When second-order temporal discretization was applied, it was observed that as the sharpening factor increased, the air layer formed predominantly along both lateral sides of the sweep angle, with minimal air layer formation in the region behind the injection hole. This trend was also evident in Case 2.3, which employed first-order temporal discretization with the highest sharpening factor. However, for cases utilizing first-order temporal discretization, a consistent trend with respect to the increase in sharpening factor was difficult to identify, as observed in Case 2.2. On the other hand, differences in the temporal discretization order influenced the smoothness of the air layer formation, as confirmed in Section 4.1. These results were also quantitatively evaluated by comparing the sweep angle with experimental results, as presented in Table 6 and Figure 9. An important observation is that increasing the sharpening factor to suppress numerical diffusion resulted in a larger diffusion angle and consequently a smaller sweep angle. This outcome appears to explain why the air layer formed predominantly along the lateral sides only. As illustrated in Figure 5, considering that the air layer formed uniformly in the experiment, it appears more appropriate to employ a second-order temporal scheme with a sharpening factor of zero to achieve stable and uniform air layer formation, rather than to increase the sharpening factor.

Furthermore, the drag reduction rates of all cases were quantitatively evaluated. As presented in Table 6 and Figure 9, when second-order temporal discretization was employed, the air layer was formed only on the lateral sides as the sharpening factor increased, resulting in a corresponding decrease in the drag reduction rate. However, when first-order temporal discretization was applied, the air layer formation exhibited somewhat irregular patterns with an increasing sharpening factor. As a result, the drag reduction rates also varied according to these irregular air layer formations. Furthermore, the wall shear stress on the flat plate varied across different cases, as depicted in Figure 8. Specifically, the variation trend of wall shear stress across different cases was consistent with the air layer formation patterns. When second-order temporal discretization was employed, regions of reduced wall shear stress progressively shifted toward the lateral sides as the sharpening factor increased. Conversely, when first-order temporal discretization was applied, no clear trend with respect to the sharpening factor could be identified.

The evaluation of cases with varying temporal discretization order and sharpening factor showed that increasing the sharpening factor caused air layer formation only on the lateral side, deviating from the experimental observations. Consequently, second-order temporal discretization with a sharpening factor of 0.0, combined with a time step of 0.001 s derived from Section 4.1, proved sufficient to replicate the experimentally observed air layer formation. Using these derived numerical parameters, the additional influence of other variables was analyzed in Section 4.3.

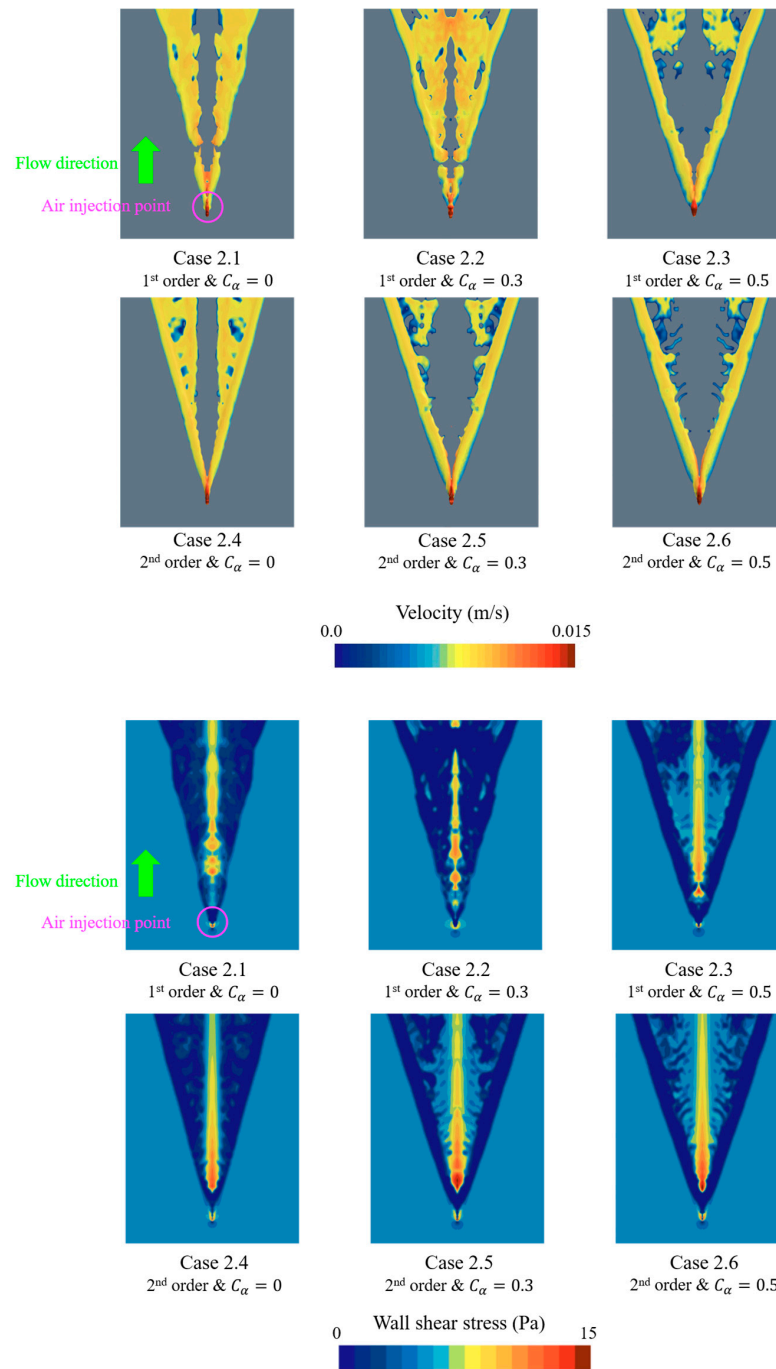


Figure 8. Effects of temporal discretization order and sharpening factor on air layer formation and shear stress on the plate.

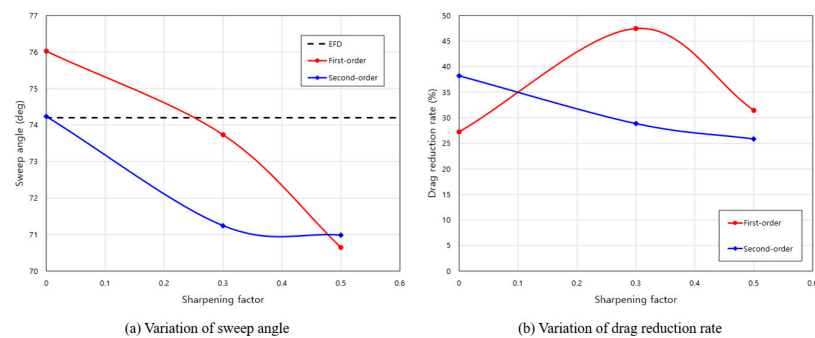


Figure 9. Variation of sweep angle and resistance reduction rate with sharpening factor.

4.3. Effects of Turbulence Model and Wall y^+

All simulations in Sections 4.1 and 4.2 were conducted using the SST $k - \omega$ turbulence model with wall y^+ values maintained above 30. However, it is necessary to investigate the effects of turbulence model selection and the wall y^+ values on air layer formation and drag reduction rate. In previous studies, simulations were performed using the SST $k - \omega$ and RST turbulence models with wall y^+ values above 30 [16,21]. To provide a more comprehensive analysis, this study evaluated six cases comprising three turbulence models of realizable $k - \epsilon$, SST $k - \omega$, and RST, each applied under two different wall y^+ conditions, i.e., “ $y^+ > 30$ ” and “ $y^+ < 1$ ”. Under these conditions, the cases were systematically subdivided as presented in Table 7, and their differences were evaluated. Furthermore, based on the results from Sections 4.1 and 4.2, the numerical settings that most closely replicated the experimental air layer formation were employed. These settings included a time step of 0.001 s, second-order temporal discretization, and a sharpening factor of 0.0. For the y^+ conditions, the total thickness of the prism layer was kept constant across all cases, while the near-wall cell thickness and the number of prism layers were adjusted to achieve the target y^+ values. This approach ensured consistent overall mesh refinement while enabling precise control of the near-wall resolution for different y^+ strategies.

Table 7. Effects of turbulence model and wall y^+ on sweep angle and resistance of a plate.

	Case 3.1	Case 3.2	Case 3.3	Case 3.4	Case 3.5	Case 3.6
Wall y^+	$y^+ > 30$	$y^+ > 30$	$y^+ > 30$	$y^+ < 1$	$y^+ < 1$	$y^+ < 1$
Turbulence model	Realizable $k - \epsilon$	SST $k - \omega$	RST	Realizable $k - \epsilon$	SST $k - \omega$	RST
Sweep angle (deg)	75.27	74.24	76.16	75.85	74.79	77.36
Error (%)	1.44	0.051	2.65	2.23	0.80	4.25
C_T	1.517×10^{-3}	1.526×10^{-3}	1.902×10^{-3}	1.436×10^{-3}	1.253×10^{-3}	1.782×10^{-3}
Drag reduction rate (%)	38.60	38.21	23.01	41.86	49.27	27.84

As illustrated in Figure 10, regarding the differences between turbulence models, the cases using the realizable $k - \epsilon$ and SST $k - \omega$ models exhibited similar trends in air layer formation, whereas the case using the RST model showed a notable difference from the other two models, with the air layer being partially formed behind the air injection hole. The more interesting point is that there were differences in air layer formation depending on the wall y^+ value. For all three turbulence models, the wall y^+ below 1 condition showed that the air layer extended further behind the injection holes, forming a denser air layer compared to the y^+ above 30 condition. Such variation becomes even more evident when examining the air layer thickness comparison presented in Figure 11. This difference can be attributed to the enhanced mesh resolution under the low y^+ condition ($y^+ < 1$). As the grid becomes finer to properly resolve the boundary layer on the flat plate, it becomes possible to capture air layers that could not be detected under y^+ above 30 conditions. Furthermore, as presented in Table 7, a quantitative comparison was conducted through sweep angle comparison with the experimental result. The results showed that, unlike the cases using the realizable $k - \epsilon$ and SST $k - \omega$ models which exhibited similar air layer formation, the cases using the RST model showed larger errors compared to the other two models. Additionally, when the same turbulence model was applied, the cases with y^+ below 1 commonly showed an increase in sweep angle and slightly larger errors compared to the experimental results than the cases with y^+ above 30.

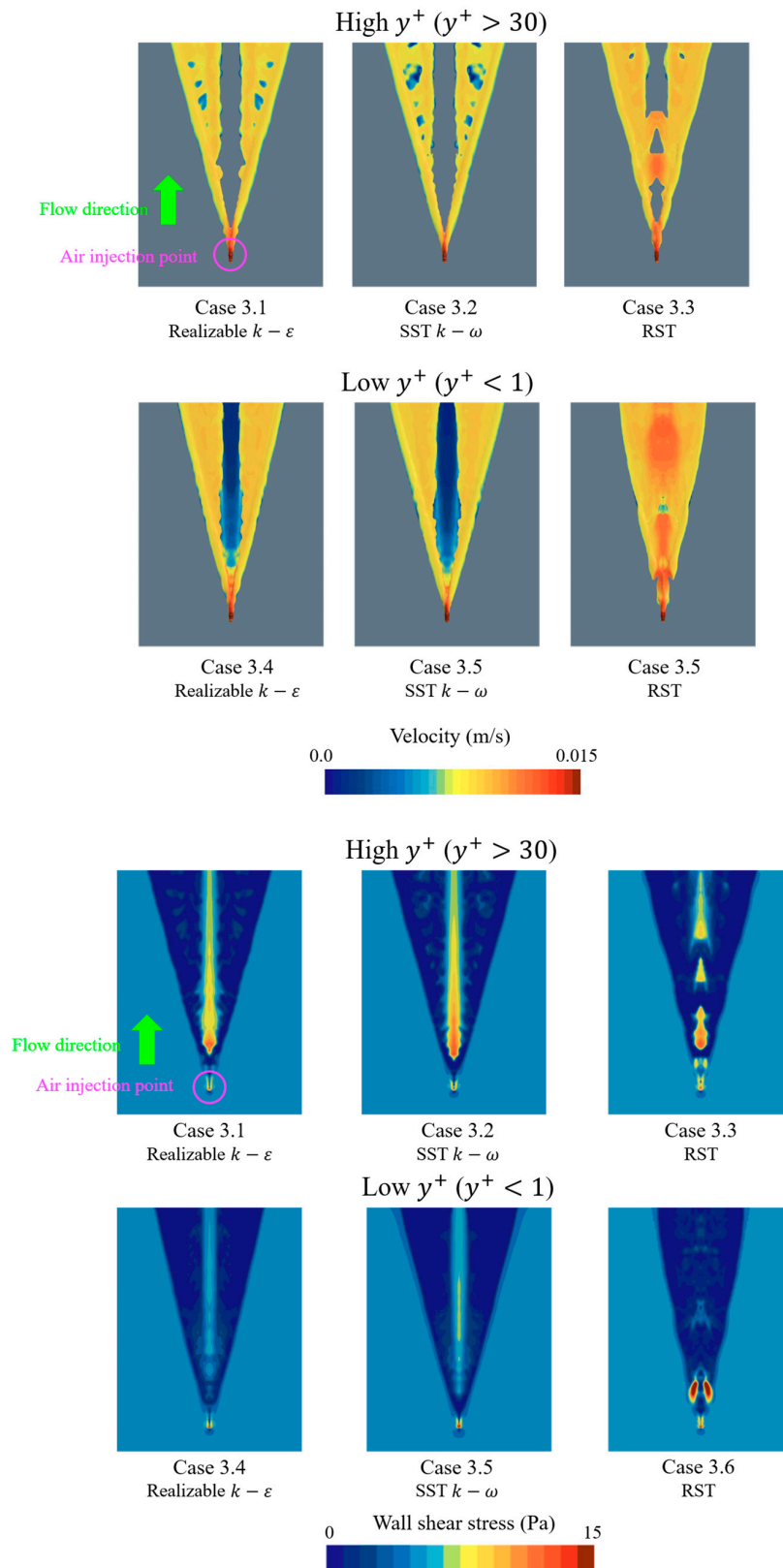


Figure 10. Effects of turbulence model and wall y^+ on air layer formation and shear stress on plate.

On the other hand, the variation in drag showed a similar trend to the variation in air layer formation. As presented in Table 7, regardless of wall y^+ conditions, the cases employing the realizable $k - \epsilon$ and SST $k - \omega$ turbulence models exhibited similar trends in drag reduction. However, the case applying the RST turbulence model showed a lower

drag reduction rate compared to the other two models. From the perspective of wall y^+ conditions, even when employing the same turbulence model, the drag reduction rate showed an increasing trend under conditions where wall y^+ was below 1. These results can be explained by changes in wall shear stress on the flat plate. As depicted in Figure 10, under low y^+ condition ($y^+ < 1$) the denser air layer formation enabled the capture of air layers that were not observed under high y^+ condition ($y^+ > 30$). Consequently, a reduction in wall shear stress was confirmed.

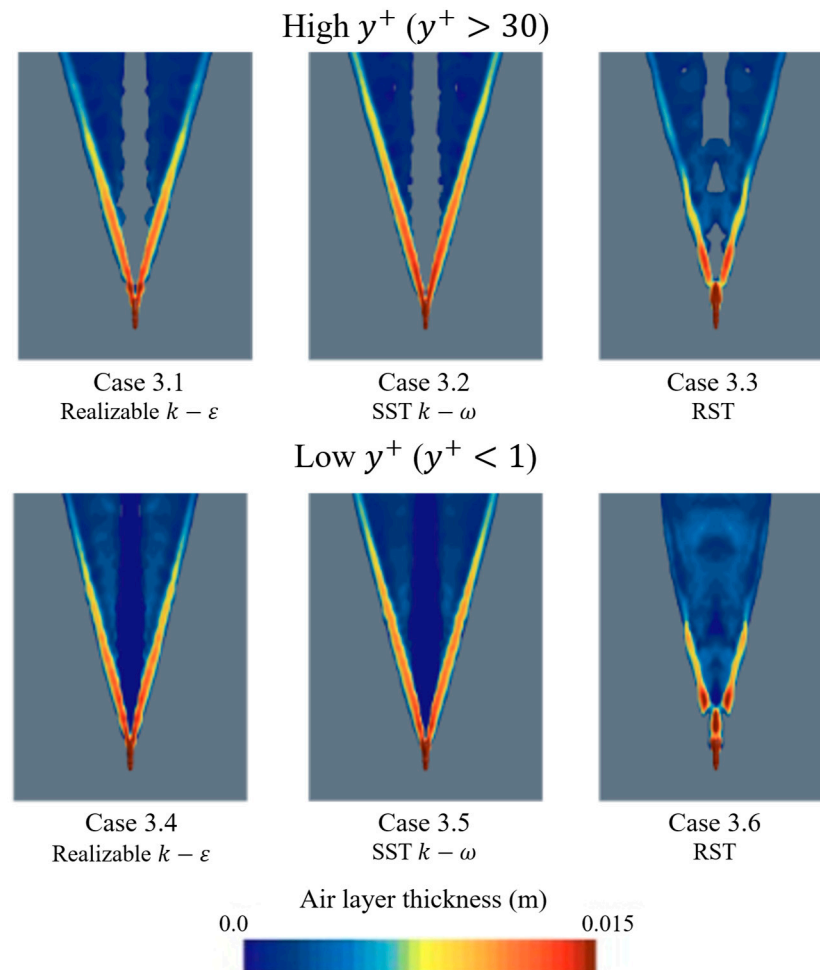


Figure 11. Variation in air layer thickness according to turbulence model and wall y^+ .

In this section, the effects of turbulence models and wall y^+ conditions were compared using the numerical parameters derived from Sections 4.1 and 4.2 that provided stable air layer formation similar to the experiment (time step of 0.001 s, second-order temporal discretization, and sharpening factor of 0.0). As a result, Case 3.2 and Case 3.5, both employing the SST $k - \omega$ turbulence model, were identified as the two most accurate cases with errors within 1% in the sweep angle evaluation. Although the high y^+ condition yielded slightly smaller errors in the sweep angle comparison, both cases showed small errors overall.

As depicted in Figure 12, comparison of air layer formation revealed that the low y^+ condition produced air layers more consistent with experimental observations. This indicates that resolving the viscous sublayer directly without wall functions, combined with the finer near-wall mesh resolution inherent to the low y^+ approach, is essential for accurately capturing air layer dynamics. Conversely, the high y^+ condition utilizes wall functions with coarser near-wall mesh, which inadequately resolves the steep gradients and interfacial instabilities critical to air layer formation.

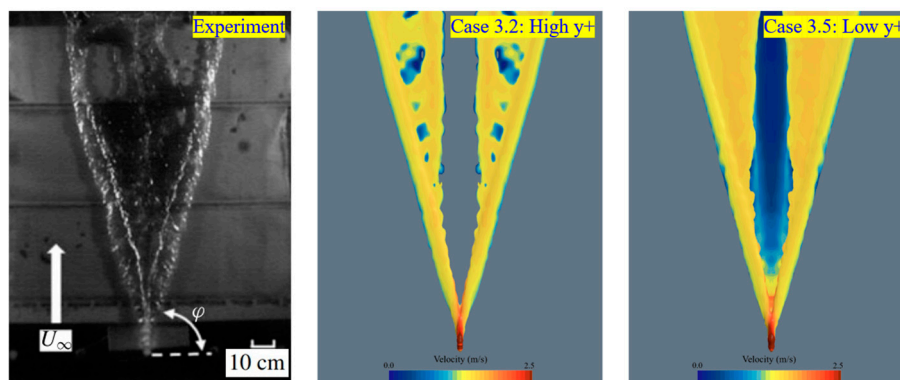


Figure 12. Comparison of air layer formation between the two most similar cases: high y^+ and low y^+ with the SST $k - \omega$ turbulence model.

5. Concluding Remarks

This study evaluates how numerical parameters affect air layer formation in CFD simulations of air lubrication systems through comparison with experimental data. In this process, Part 1 assessed the influence of time step and temporal discretization order through systematic comparison of different cases. In Part 2, based on the results from Part 1, the effects of temporal discretization order and sharpening factor for reducing numerical diffusion were analyzed using the time step value that could form a stable air layer. Finally, based on Parts 1 and 2, the influence of turbulence model and wall y^+ condition was evaluated. Through this sequential approach across Parts 1, 2, and 3, a one-factor-at-a-time methodology was employed to isolate and clearly identify the individual effects of each numerical parameter. While interactions between parameters may exist, investigating all possible combinations would require an excessively large number of cases. Therefore, the scope of this study was defined to focus on understanding the isolated influence of each key parameter, thereby providing fundamental guidelines for ALS CFD simulations. The results can be summarized as follows:

- Part 1: From the comparison of time step and temporal discretization order, it was confirmed that the first-order scheme required a smaller time step of 0.0005 s for stable air layer formation, while the second-order scheme achieved stability at the relatively larger time step of 0.001 s.
- Part 2: From the evaluation of numerical diffusion by varying temporal discretization order and sharpening factor, it was found that reducing numerical diffusion by increasing the sharpening factor resulted in air layer formation only on the lateral sides. Between the first-order and second-order temporal discretization, the second order was found to form a smoother air layer, making it more appropriate. Given this phenomenon with the sharpening factor, applying second-order temporal discretization alone was considered sufficient.
- Part 3: From the comparison of realizable $k - \epsilon$, SST $k - \omega$, and Reynolds stress transport (RST) turbulence models under conditions of wall $y^+ > 30$ and wall $y^+ < 1$, the SST $k - \omega$ turbulence model was found to be the most similar to the experimental results. Moreover, under wall $y^+ < 1$ condition, an air layer that was not captured at high y^+ was formed and represented more similarly to the experiment. This is attributed to the finer mesh resolution near the flat plate, indicating that the low wall y^+ condition is appropriate for implementing an ALS through CFD.

Furthermore, the simulations under these different wall y^+ conditions both obtained reliability through grid convergence tests.

The results of this study provide a fundamental basis for implementing an ALS through CFD. These numerical settings can serve as a guide for implementing an ALS

using commercial programmes. However, the present study has limitations because it used a flat plate with a single injection hole, whereas an actual ALS involves ships with multiple injection holes arranged in a slit configuration. Therefore, direct application of these findings to real-ship scenarios requires additional validation and consideration of the effects of multi-hole interactions and three-dimensional hull curvature. Furthermore, this study employed RANS-based turbulence models, which have inherent limitations in capturing instantaneous interface instabilities at the gas–liquid interface. Although more computationally expensive, advanced methods such as Large Eddy Simulation (LES) and Detached Eddy Simulation (DES) are expected to provide better resolution of the air layer dynamics and interfacial phenomena. Nevertheless, the findings of this study can serve as a benchmark for CFD practitioners when in establishing numerical settings for ALS simulations. Based on these findings, future work is planned to observe the changes when applying multiple injection ports in a slit configuration on ship hulls, as well as to employ advanced turbulence modelling techniques such as LES and DES to better capture the unsteady interfacial dynamics of the air layer.

Author Contributions: Conceptualization, S.S.; Methodology, G.M. and S.S.; Software, G.M. and K.J.; Validation, G.M.; Formal analysis, G.M., H.Y. and Y.D.; Investigation, G.M., H.Y. and S.S.; Data curation, G.M., K.K. and K.J.; Writing—original draft, G.M.; Writing—review & editing, S.D., M.A., D.K., S.K. (Seungnam Kim), S.K. (Sanghyun Kim) and S.S.; Visualization, G.M. and S.S.; Supervision, S.S.; Project administration, S.K. (Sanghyun Kim) and S.S.; Funding acquisition, S.S. All authors have read and agreed to the published version of the manuscript.

Funding: This research was funded by Inha University Research Grant.

Data Availability Statement: The original contributions presented in this study are included in the article. Further inquiries can be directed to the corresponding authors.

Conflicts of Interest: The authors declare no conflict of interest.

Appendix A

In Appendix A, additional data have been incorporated to supplement the data in the manuscript and enhance reader comprehension.

Table A1. Grid convergence study and numerical uncertainty analysis (Wall $y^+ > 30$).

Parameter	Sweep Angle (deg)	C_T
N_1	3,039,828	3,039,828
N_2	2,096,642	2,096,642
N_3	1,183,389	1,183,389
r_{21}	1.45	1.45
r_{32}	1.77	1.77
ϕ_1 (Fine)	74.24	1.525×10^{-3}
ϕ_2 (Medium)	73.83	1.511×10^{-3}
ϕ_3 (Course)	75.61	1.635×10^{-3}
ϵ_{32}	1.771	1.249×10^{-4}
ϵ_{21}	−0.403	1.523×10^{-5}
s	−1	−1
e_a^{21}	5.422×10^{-3}	9.982×10^{-3}
q	−0.442	−0.666
p_a	2.798	3.869
ϕ_{ext}^{21}	74.45	1.531×10^{-3}
e_{ext}^{21}	2.957×10^{-3}	3.100×10^{-3}
GCI_{fine}	0.37%	0.39%

Table A2. Grid convergence study and numerical uncertainty analysis (Wall $y^+ < 1$).

Parameter	Sweep Angle (deg)	C_T
N_1	4,412,050	4,412,050
N_2	2,572,342	2,572,342
N_3	1,155,243	1,155,243
r_{21}	1.72	1.72
r_{32}	2.23	2.23
ϕ_1 (Fine)	74.79	1.253×10^{-3}
ϕ_2 (Medium)	74.87	1.256×10^{-3}
ϕ_3 (Course)	76.16	1.364×10^{-3}
ϵ_{32}	1.291	1.083×10^{-4}
ϵ_{21}	0.0745	3.128×10^{-6}
s	1	1
e_a^{21}	9.95×10^{-4}	9.982×10^{-3}
q	1.0003	-1.2025
p_a	3.433	4.341
ϕ_{ext}^{21}	74.78	1.253×10^{-3}
e_{ext}^{21}	1.854×10^{-3}	2.656×10^{-4}
GCI_{fine}	0.02%	0.03%

References

1. IMO. 2023 IMO Strategy on Reduction of GHG Emissions from Ships. 2023. Available online: <https://www.imo.org/en/ourwork/environment/pages/2023-imo-strategy-on-reduction-of-ghg-emissions-from-ships.aspx> (accessed on 25 December 2025).
2. Li, C.; Wang, H.; Sun, P. Numerical investigation of a two-element wingsail for ship auxiliary propulsion. *J. Mar. Sci. Eng.* **2020**, *8*, 333. [CrossRef]
3. Chou, T.; Kosmas, V.; Acciaro, M.; Renken, K. A comeback of wind power in shipping: An economic and operational review on the wind-assisted ship propulsion technology. *Sustainability* **2021**, *13*, 1880. [CrossRef]
4. Guzelbulut, C.; Suzuki, K. Optimal design of rotor sails based on environmental conditions and cost. *J. Mar. Sci. Eng.* **2023**, *12*, 31. [CrossRef]
5. Spinelli, F.; Mancini, S.; Vitiello, L.; Bilandi, R.N.; De Carlini, M. Shipping decarbonization: An overview of the different stern hydrodynamic energy saving devices. *J. Mar. Sci. Eng.* **2022**, *10*, 574. [CrossRef]
6. Mizokami, S.; Kawakado, M.; Kawano, M.; Hasegawa, T.; Hirakawa, I. Implementation of ship energy-saving operations with Mitsubishi air lubrication system. *Mitsubishi Heavy Ind. Tech. Rev.* **2013**, *50*, 44–49.
7. Mäkiharju, S.A.; Perlin, M.; Ceccio, S.L. On the energy economics of air lubrication drag reduction. *Int. J. Nav. Archit. Ocean. Eng.* **2012**, *4*, 412–422. [CrossRef]
8. Mizokami, S.; Kawakita, C.; Kodan, Y.; Takano, S.; Higasa, S.; Shigenaga, R. Experimental study of air lubrication method and verification of effects on actual hull by means of sea trial. *Mitsubishi Heavy Ind. Tech. Rev.* **2010**, *47*, 41–47.
9. Kim, Y.-R.; Steen, S. Potential energy savings of air lubrication technology on merchant ships. *Int. J. Nav. Archit. Ocean. Eng.* **2023**, *15*, 100530. [CrossRef]
10. An, H.; Pan, H.; Yang, P. Research progress of air lubrication drag reduction technology for ships. *Fluids* **2022**, *7*, 319. [CrossRef]
11. Chillemi, M.; Raffaele, M.; Sfravara, F. A Review of Advanced Air Lubrication Strategies for Resistance Reduction in the Naval Sector. *Appl. Sci.* **2024**, *14*, 5888. [CrossRef]
12. Pavlov, G.A.; Yun, L.; Bliault, A.; He, S.-L. *Air Lubricated and Air Cavity Ships*; Springer: Berlin/Heidelberg, Germany, 2020.
13. Mäkiharju, S.A.; Lee, I.-H.R.; Filip, G.P.; Maki, K.J.; Ceccio, S.L. The topology of gas jets injected beneath a surface and subject to liquid cross-flow. *J. Fluid Mech.* **2017**, *818*, 141–183. [CrossRef]
14. Jang, J.; Choi, S.H.; Ahn, S.-M.; Kim, B.; Seo, J.S. Experimental investigation of frictional resistance reduction with air layer on the hull bottom of a ship. *Int. J. Nav. Archit. Ocean. Eng.* **2014**, *6*, 363–379. [CrossRef]
15. Park, S.H.; Lee, I. Optimization of drag reduction effect of air lubrication for a tanker model. *Int. J. Nav. Archit. Ocean. Eng.* **2018**, *10*, 427–438. [CrossRef]
16. Kim, H.-T.; Kim, H.; Lee, D.-Y. Study on the Skin-frictional Drag Reduction Phenomenon by Air Layer using CFD Technique. *J. Soc. Nav. Archit. Korea* **2019**, *56*, 361–371. [CrossRef]
17. Shademani, R.; Mikkola, T.; Manderbacka, T.; Remes, H.; Tavakoli, S. CFD Modeling of Air Lubrication Systems in Ships. In Proceedings of the Numerical Towing Tank Symposium, Mulheim, Germany, 23–25 October 2024.

18. Fotopoulos, A.G.; Margaris, D.P. Computational Analysis of Air Lubrication System for Commercial Shipping and Impacts on Fuel Consumption. *Computation* **2020**, *8*, 38. [[CrossRef](#)]
19. Uppal, H.; Kumar, J.R.; Srinivas, K.S.; Dhavalikar, S.S. Numerical Assessment of Air Lubrication System for Tanker. In *7th International Conference on Ship and Offshore Technology (ICSOT INDIA 2023) Proceedings*; The Royal Institution of Naval Architects: London, UK, 2023; pp. 128–141.
20. Abbas, N.; Hawa, R.; Hatem, W. Drag Reduction and EEXI Compliance: Evaluating Air Lubrication for In-Service Ships via CFD. Polish Maritime Research 2025. Available online: <https://yadda.icm.edu.pl/baztech/element/bwmeta1.element.baztech-b7c13738-549e-44c5-8e38-4289657bcf6e> (accessed on 25 December 2025).
21. Kim, D.-Y.; Ha, J.-Y.; Paik, K.-J. Numerical Study on the Extrapolation Method for Predicting the Full-scale Resistance of a Ship with an Air Lubrication System. *J. Ocean. Eng. Technol.* **2020**, *34*, 387–393. [[CrossRef](#)]
22. Doğrul, A.; Arıkan, Y.; Celik, F. A numerical investigation of air lubrication effect on ship resistance. In *Proceedings of the International Conference on Ship Drag Reduction, Istanbul, Turkey, 20–21 May 2010*.
23. Kim, H.-T.; Kim, H.-T.; Kim, J.-J.; Lee, D.-Y. Study on the skin-friction drag reduction by air injection using computational fluid dynamics-based simulations. In *Practical Design of Ships and Other Floating Structures*; Springer: Berlin/Heidelberg, Germany, 2019; pp. 205–226.
24. Kim, H.-T.; Kim, H.-T.; Kim, H.-J.; Kim, J.-J. Study on the Evaluation of Frictional Drag Reduction by Air Lubrication and the Arrangement of Air Injection Parts for a Liquefied Natural Gas Carrier. *J. Soc. Nav. Archit. Korea* **2021**, *58*, 144–157. [[CrossRef](#)]
25. Ferziger, J.H.; Perić, M.; Street, R.L. *Computational Methods for Fluid Dynamics*; Springer: Berlin/Heidelberg, Germany, 2019.
26. Celik, I.B.; Ghia, U.; Roache, P.J.; Freitas, C.J. Procedure for estimation and reporting of uncertainty due to discretization in CFD applications. *J. Fluids Eng.* **2008**, *130*, 078001. [[CrossRef](#)]
27. Siemens Digital Industries Software. *Simcenter STAR-CCM+ User Guide*, Version 19.06.008; Siemens Digital Industries Software: Plano, TX, USA, 2024.

Disclaimer/Publisher’s Note: The statements, opinions and data contained in all publications are solely those of the individual author(s) and contributor(s) and not of MDPI and/or the editor(s). MDPI and/or the editor(s) disclaim responsibility for any injury to people or property resulting from any ideas, methods, instructions or products referred to in the content.